Fifth International Conference on CFD in the Process Industries
CSIRO, Melbourne, Australia
13-15 December 2006

A CFD STUDY OF FLUID-PARTICLE BEHAVIOUR IN A POROUS VESTIBULE OF A HUMAN NASAL AND PHARYNX AIRWAY

H.F. Li[1], J.Y. TU[1], D.K. SHANMUGAM[1], C.L. XUE[2] and C.G. LI[2]

[1]School of Aerospace, Mechanical and Manufacturing Engineering, RMIT University, Australia

[2] School of Health Sciences, RMIT University, Australia

ABSTRACT

A CFD approach to predict the airflow behaviours and particle deposition efficiency through an inertial and viscous regime in a porous model vestibule region of the human nasal cavity is described. Deposition efficiency in the nasal cavity and pharynx was calculated for particles of diameter between 0.5 and 100μm under constant inspiratory flow rate of 12 l/min. It was found that the inclusion of porous region in the nasal vestibule region contributes to a significant increase in the deposition efficiency as well as causing a forward shift in the area averaged velocity pattern of the fluid. This forward shift in the pattern leads to a shift in the local particle deposition when compared to the non-porous model. Information on the deposition efficiency of aerosol particles in the human nasal airways is used for both optimizing the delivery of therapeutic aerosols into the nose and risk assessment of toxic airborne pollutants inhaled through the nose into the respiratory system.

INTRODUCTION

The ever increasing awareness of environmental pollution problems associated with breathing in humans require a better understanding of the dynamics and spatial distribution of the transport processes in the nasal cavity. The anatomy of the nose plays a significant role in these processes. Approximately 15 mm from the nostrils is the narrowest portion of the entire airway, of which the nasal valve accounts for approximately 50% of the total resistance to respiratory airflow from the nostrils to the throat. This restriction is caused by the presence of nasal hair as well the geometry itself. The nasal hair inside the vestibule occupies 20 to 40 % of volume (Mygind and Dahl, 1998). The main function of these is to filter very small particles (<0.01μm) and very large particles (>5μm) (Cheng et al., 2001).

As has been established in previous research, CFD is a very useful tool in formulating a study into the engineering perspective of biological problems (Naftali et al., 1998). To this end, several numerical simulations have been performed to characterize flows in the upper respiratory tract. Early research by Schreck et al. (1993) established a correlation between flow resistance and the geometry of the human nose. Balashazy et al. (1993) studied the particle deposition in an airway bifurcation model. This work was extended by Hoffmann et al. (2003) for inspiratory deposition of ultra-fine particles. Mortonen et al. (2002) simulated the human upper respiratory tract with a model based on the computer-reconstructed images of a silicone rubber cast of the human throat, trachea and main bronchi. Stapleton et al. (2000) numerically studied aerosol deposition in the mouth and throat. They chose to create an average geometrical model of the airways based on data from Computed Tomography (CT) scans, Magnetic Resonance Imaging (MRI) scans, and direct observation of living subjects. In their study, the disperse phase was modelled using one-way coupling (the particles do not influence the gas flow) with a Lagrangian trajectory model. However, they recognised that the use of k-ε turbulence model for the complex nasal cavity geometry proved to be erroneous when compared to experimental observation.

Zhang et al. (2002) modelled particle deposition under transitional and turbulent flow in a simplified model including the trachea, larynx, pharynx, and oral cavity. They found that turbulence increases particle deposition after the laryngeal constriction and that the top and bottom zone of the inlet plane corresponds to particles that deposit more frequently. Gemci et al. (2000, 2002a) numerically studied an inhalation flow containing a medicinal spray passing through a simple model of the larynx and trachea. The geometric inaccuracy of this model meant less deposition was predicted than for more accurate models.

Thus, given a brief overview of the research related to this study, it can be seen that no research has been carried out to consider the effect of the nasal hair on particle deposition. It was assumed by Hahn et al. (1993) that the inclusions would not contribute to the difference in the particle deposition efficiency. But in nature, the main function of the nasal hair is to act as a filter for very small and very large particles (Mygind and Dahl, 1998). However the geometrical construction of nasal hair throughout the vestibule would be hypothetical as the distribution of nasal hairs varies from person to person. Another drawback is that it is time consuming and hence not feasible to simulate. Nevertheless, a simple alternative method of simulating the nasal hair is to consider them a filtration medium.

Research has been carried out by using a porous medium for filtration purposes in many industrial applications such as soil pollution, deep-bed filtration, and fluidised beds including flows through packed beds, oil recovery and geothermal energy (Frey et al., 1999). But the inclusion of the porous medium for emulating the hair growth has not been considered by any researchers. Since the impact of hair growth would be important for a real anatomical nasal cavity study, the inclusion of a porous medium in the vestibule region was considered. Therefore this research aims both qualitatively and quantitatively to study the impact of emulation of the nasal hair using the porous medium and to highlight the implications of this effect. Another aim of this research is

to show how CFD can be applied as a tool to visualise and demonstrate the basic features of this technique and how it can be used to further optimise the drug delivery process.

METHODOLOGY

Mesh Generation

Slice images were obtained from an MRI scan and the outlines of each slice were extracted. The extracted outlines were then used to form a core for the CAD geometry. A three-dimensional surface and then volume was generated from the segmented data. The geometry was smoothened to eliminate all discrete portions and to minimize sharp corners. This was an iterative process. The recreated geometry as shown in Figure 1(a) was then discretized by the finite volume approach to obtain Figure 1(b). The mesh was refined from very coarse to fine until a better convergence was achieved. In other words, an optimal volume mesh was used to minimize time required for computation without compensating the accuracy. These mesh adaptations were carried out using the pre-processor GAMBIT. Due to problems in visualising a very fine mesh, only a coarse mesh is pictured in Figure 1(b). Although the solution of generating the mesh seems straight forward, considerable effort was made to exactly replicate the real nasal cavity and throat. Figure 1(c) shows the divided zones and sections of the model, which were used to predict the particle deposition and fluid-particle velocity.

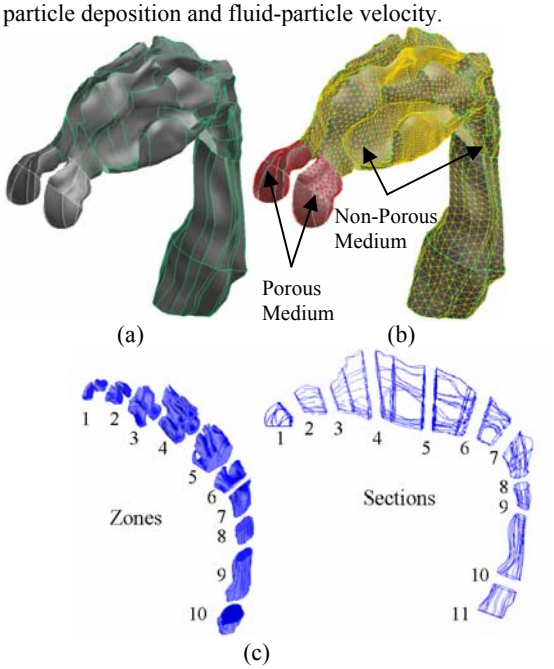

Figure 1. (a) CAD geometry of the recreated CT slice data; (b) Coarse mesh generated from the CAD geometry; (c) Nasal Cavity and Pharynx model split into 10 Zones and 11 Sections.

Numerical Model

CFD simulation of the model was computed by solving the Navier-Stokes equations in a three-dimensional grid with FLUENT code (2003). In this research FLUENT computer code was used to predict the Lagrangian particle tracking using the Discrete Phase Model (DPM) (Dukowicz, 1980). In the Lagrangian model, the fluid phase is solved by Eulerian equations, and then the Lagrangian equations of motion are integrated for the dispersed phase.

The equation for the conservation of mass, or continuity equation, can be written as

$$\frac{\partial \rho}{\partial t} + \nabla \cdot \left(\rho \vec{\upsilon} \right) = 0 \qquad (1)$$

Conservation of momentum can be described as

$$\frac{\partial}{\partial t}(\rho \vec{\upsilon}) + \nabla \cdot (\rho \vec{\upsilon} \vec{\upsilon}) = -\nabla p + \nabla \cdot (\bar{\bar{\tau}}) + \rho \vec{g} + \vec{F} \qquad (2)$$

where p is the static pressure, $\bar{\bar{\tau}}$ is the stress tensor, and $\rho \vec{g}$ & $\vec{F}$ are the gravitational body force and external body forces respectively. $\vec{F}$ also contains other model-dependent source terms such as porous-media and user-defined sources (detailed in Equation 10).

The stress tensor $\bar{\bar{\tau}}$ is given by

$$\bar{\bar{\tau}} = \mu \left[(\nabla \vec{\upsilon} + \nabla \vec{\upsilon}^{\mathrm{T}}) - \frac{2}{3} \nabla \cdot \vec{\upsilon} I \right] \qquad (3)$$

where μ is the molecular viscosity, I is the unit tensor, and the second term on the right hand side of Equation (3) is the effect of the volume.

This research is novel as hair in the vestibule region is considered .This implies that the model could be treated as a porous media model. This incorporates an empirically determined flow resistance in a region of the model. Fundamentally the porous media model is nothing more than an added momentum sink in the governing momentum equations.

Porous media was modelled by the addition of a momentum source term to the standard fluid flow equations.

$$S_i = -\left(\sum_{j=1}^{3} D_{ij} \mu \upsilon_j + \sum_{j=1}^{3} C_{ij} \frac{1}{2} \rho \upsilon_{mag} \upsilon_j \right) \qquad (4)$$

The source term S_i for the i^{th} (x, y or z) is composed of two parts: a viscous loss term (Darcy's law, the first term on the right-hand side of Equation 4), and an inertial loss term (the second term on the right-hand side of Equation 4), where ρ is the total mass density of species, υ_{mag} and υ_j is the fluid velocity, μ is the viscosity of the fluid, D and C are the prescribed diagonal matrices. This momentum sink contributes to the pressure gradient in the porous cell, creating a pressure drop that is proportional to the fluid velocity (or velocity squared) in the cell. With a homogeneous porous media Equation (4) can be reduced to Equation (5).

$$S_i = -\left(\frac{\mu}{\alpha} \upsilon_i + C_2 \frac{1}{2} \rho \upsilon_{mag} \upsilon_i \right) \qquad (5)$$

where α is the permeability and C_2 is the inertial resistance factor.

For the case of 12 l/min (for the resting condition), the velocity is at 1.29m/s, the flow is found to be laminar (Hahn et al, 1993) and therefore for laminar flow through porous media, the pressure drop is typically proportional to velocity and the constant C_2 can be considered to be zero. Ignoring convective acceleration and diffusion, the porous media model then reduces to Darcy's Law (Frey et al., 1999)

$$\nabla p = -\frac{\mu}{\alpha}\vec{\upsilon} \quad (6)$$

Another significant consideration in formulating the porous media equation is the true velocity inside the porous medium. In nature the non-porous region has a uniform (superficial) velocity inside a medium unless it is affected by factors such as geometry, gravitational, shear, inertial or viscous forces. However, the porous medium has a volume restriction in addition to the non-porous medium forces. Therefore the increased velocity inside the porous medium was taken into account for the model. The superficial velocity in the governing equations can be represented as

$$\vec{\upsilon}_{superficial} = \gamma \vec{\upsilon}_{physical} \quad (7)$$

where γ is the porosity of the media and is defined as the ratio of the volume occupied by the fluid to the total volume of the geometry.

Using the physical velocity formulation, and assuming a general scalar ϕ, the governing equation in an isotropic porous media has the following form:

$$\frac{\partial(\gamma\rho\phi)}{\partial t} + \nabla\cdot\left(\gamma\rho\vec{\upsilon}\phi\right) = \nabla\cdot\left(\gamma\Gamma\nabla\phi\right) + \gamma S_\phi \quad (8)$$

Assuming isotropic porosity and single phase flow, the volume-averaged mass and momentum conservation equations are:

$$\frac{\partial(\gamma\rho)}{\partial t} + \nabla\cdot\left(\gamma\rho\vec{\upsilon}\right) = 0 \quad (9)$$

$$\frac{\partial\left(\gamma\rho\vec{\upsilon}\right)}{\partial t} + \nabla\cdot\left(\gamma\rho\vec{\upsilon}\vec{\upsilon}\right) = -\gamma\nabla p + \nabla\cdot\left(\gamma\vec{\tau}\right) + \gamma\vec{B}_f - \left(\frac{\mu}{\alpha} + \frac{C_2\rho}{2}\left|\vec{\upsilon}\right|\right)\vec{\upsilon} \quad (10)$$

The last term in Equation (10) represents the viscous and inertial drag forces imposed by the pore walls on the fluid.

The Discrete Phase Model (DPM) was used to trace the dispersion of particles about the trajectory. The Lagrangian scheme is most popular in engineering applications for the prediction of particulate flows because it can easily be combined with a stochastic scheme, albeit with high computational costs (Tu, 2000). Trajectories of individual particles can be tracked by integrating the force balance equations on the particle.

$$\frac{du_p}{dt} = F_D\left(u_g - u_p\right) + \frac{g(\rho_p - \rho_g)}{\rho_p} \quad (11)$$

$F_D(u_g\text{-}u_p)$ is the drag force per unit particle mass where

$$F_D = \frac{18\mu_g}{\rho_p d_p^2}\frac{C_D\,\mathrm{Re}_p}{24} \quad (12)$$

Where ρ_p denotes the density of particle material and d_p is the particle diameter, u_p presents the particle velocity. Re_p is the particle Reynolds number defined as

$$\mathrm{Re}_p = \frac{\rho_p d_p\left|u_p - u_g\right|}{\mu_g} \quad (13)$$

The drag coefficient C_D is given as

$$C_D = a_1 + \frac{a_2}{\mathrm{Re}_p} + \frac{a_3}{\mathrm{Re}_p^2} \quad (14)$$

where a represents the different empirical constants for smooth spherical particles over several ranges of particle Reynold's numbers (Morsi and Alexander, 1972). The particle phase defined is sufficiently dilute and particle-particle interactions and the effects of the particle volume fraction on the gas phase are negligible, thus one way coupling is used.

Numerical Procedures

In this work, analysis of air flow and particle deposition was predicted using a generic commercial code, Fluent 6.1. In using this code a segregated numerical solver method with implicit formulation and steady state time was adopted. By this approach, the equations for the conservation of mass and momentum were solved sequentially, i.e. segregated from one another. The solution was controlled by the semi-implicit method for pressure linked equations (SIMPLE). The fluid properties were first updated by an initialised solution, i.e., before the second order upwind momentum equations are solved using current values for pressure and face mass fluxes to update the velocity field. A pressure correction equation is then solved to obtain the necessary corrections to the pressure and velocity fields and the face mass fluxes such that continuity is satisfied.

For low volume fraction, the coupling between the solid phase and the fluid phase is found to be weak (Mortonen et al., 2002). Therefore the inter-phase coupling was excluded in order to increase the speed of the calculation. Finally, a check for convergence of the equation set was made, and iterations stoped when the convergence criteria is fulfilled. Otherwise, the fluid properties were updated, based on the current solution, and the steps were continued until the convergence criteria was met. The individual particles were tracked using the Discrete Phase Model (DPM) with a spherical drag law. In this method the particles were considered as the discrete phase and the fluid as the continuous phase. In other words the fluid phase is solved by Eulerian equations, and was then integrated with the Lagrangian equations of motion for the dispersed phase, tracking individual particles through the flow field.

Simulation Inlet Conditions

Mono-size droplets ranging between 0.5 and 100μm in droplet diameter were coupled (one-way) with air as the carrier gas for the simulations. The size of the particles corresponds to the range from tobacco smoke to allergy causing pollens. The coupled simulation was performed with the FLUENT code for a flow rate of 12 l/min, an approximate adult resting condition. The only medium accelerating the particles is air, and was assumed that the carrier gas (air) and the particles travel at the same inlet velocity. In order to calculate the particle deposition the particles were assumed to be captured as they hit the wall. This assumption was validated by the presence of the mucosal layer. The particles were injected from the entire inlet surface and the effects of deposition were calculated.

The most important factor in this research is the addition of porous media in the vestibule region. It is found from the nasal cavity physiology (Mygind and Dahl, 1998) that approximately 20% of the vestibule region is composed of nasal hairs and in extreme cases it is found to be of 40% by volume. Therefore a simple porosity assumption of 0.6 was considered, where the porosity is the measure of the volume open to the total volume for the fluid flow.

RESULTS AND DISCUSSIONS

Velocity variations and deposition of a series of mono-disperse aerosol injections in air for the nasal cavity and pharynx were numerically analysed at inspiration conditions. At normal breathing condition the volume fluxes were found to be 12 l/min with the Reynolds number based on the hydraulic diameter at the nostril. From the findings of the experimental study (Hahn et al, 1993) for the velocity distributions of 12 l/min, laminar flow was assumed. In analysing the results, it was deemed to be appropriate to present both qualitative and quantitative results through comprehensive parametric simulation conditions.

Particle Behaviours

At inspiration, particles injected at a velocity equal to the carrier gas (air) were investigated for their deposition along the domain to give a qualitative visualisation. This was then quantified to predict the velocity behaviour for varying particle sizes. Figure 2(a) and 2(b) shows the particle deposition from the inlet of the left and right nostril through the nasal cavity and pharynx. The discrete phase particles were injected at each node from the surface and by tracking the individual particles it can be seen that particles closer to the boundary are more likely to deposit frequently than particles injected towards the centreline of the model. In vivo, it was observed that more particles were found along the centreline of the fluid flow and fewer particles were found in the vestibule region (Figure 2(a)).

It can be seen from Figure 2(b) that as the porosity is decreased, more particles are deposited in the anterior portion of the nasal cavity. Most of the particles were found to be deposited in the vestibule region. Particles in the turbinate region were strongly influenced by the recirculation zone; these cause the particles to deposit in the superior turbinate regions. Greater discussion is presented later in the particle deposition results.

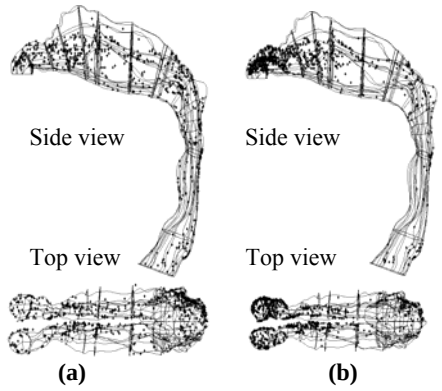

Figure 2. Particle deposition of a laminar flow inside the domain for a particle diameter of 5μm: (a) non-porous; (b) porosity of 0.6.

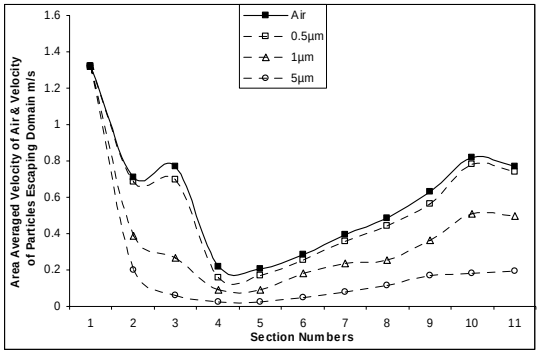

(a)

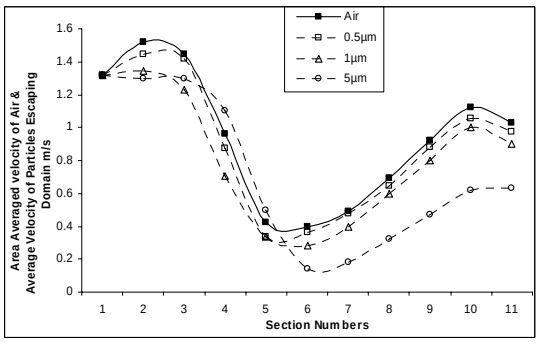

(b)

Figure 3. Velocity profiles of carrier gas and particles for a laminar flow: (a) Non-porous; (b) 60% volume open that is porosity of 0.6.

Velocity Patterns

Representative results of the distribution of the air and particle velocity through the entire domain averaged by area are shown in Figure 3. As shown in Figure 1(c), the domain was split into 11 sections and the measured velocity was plotted. This study aims to present a comparative study of the particle and gas velocities and the impact of inertial and viscous loss of the various sized mono-disperse particles during their acceleration and deceleration. Though at inlet conditions air and particles travel at same velocity, the change in the velocity of the carrier gas causes a change in the particle velocity.

An important observation comes from the fact that the inclusion of porous regime in the vestibule region causes an increase in velocity from zone 1 to zone 2, wherein the velocity tend to decrease for non-porous flow. This change in area averaged air velocity is due to the impact of the momentum sink generated by the porous model. One of the questions answered through this analysis was that the change in the inlet velocity (within laminar flow) through a non-porous medium does not contribute to a change in velocity pattern given the bend between zone 1 and zone 2, but is only influenced by the addition of porous media. In all cases the velocity decreases as air enters zone 3 and zone 4. This was however due to two reasons, the volume expansion of the domain structure and the recirculation dominant on the olfactory region. The velocity increases as the domain volume contracts and attains maximum velocity in the pharynx at section 10, where, abrupt volume shrinkage occurs.

Particle velocity behaviour compared with fluid velocity is displayed in Figure 3. With an increase in particle size,

particles exhibit deviating trendlines when compared to the carrier gas. For both the porous and non-porous models the 0.5µm particles follow the exact path of the carrier gas. This shows that there is enough energy in the carrier gas to accelerate the particles and that the particles diffuse completely with the gas. But as the particle size was increased, the energy within the carrier gas becomes insufficient to lift the particles, thereby causing an inertial loss. That is, large particles have higher inertial momentum that increases with the cube of the diameter (volume for constant density) dominating an increase in the square of the diameter (A_p) corresponding to the drag force. Large particles does not reach the same maximum velocity as that of smaller particles, however once they are directed towards the wall they are deposited. Similarly, due to the fluid flow, smaller particles are directed towards the anterior region of the wall. However, the weaker fluid flow is able to redirect many of the smaller particles away from the wall and into the central domain.

At a few instances, it was found that the particle velocity surpassed the carrier gas velocity. This phenomenon was due to the density difference between the carrier gas and the particles. The carrier gas as it enters zone 3 and zone 4 expands rapidly to fill the domain due to its lower density. But for the particles, due to higher density, the inertial force is still dominant and therefore takes additional time to show a decrease in velocity. Again, as the gas velocity tends to increase from zone 5 onwards, it accelerates the particles, however due to its low velocity, a high inertial loss becomes prominent and therefore there exists a high velocity difference.

Particle Deposition Efficiency

Particle deposition efficiencies in an anatomically real nasal cavity and pharynx are shown in Figure 4. As shown in Figure 1(c) the domain was divided into 10 zones and the deposition predicted for particles of 0.5µm to 10µm. These results obtained suggest that the deposition of particles in the range of 0.5µm to 10µm is more dependent upon the porous regime incorporated into the model. This is indirectly caused by the lower porosity leading to a lower hydraulic volume, in which the fluid flows. This volume restriction enforces a high momentum sink, thereby resulting in an increased physical velocity. This increase in velocity accelerates the particles, thereby causing the particles to deposit on to the walls.

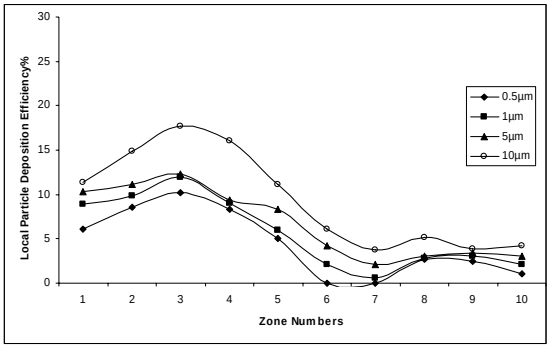

(a)

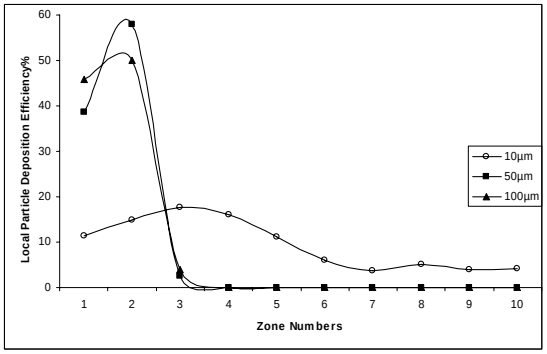

(b)

Figure 4. Local particle deposition efficiency for a laminar flow: (a) porosity = 0.6; (b) porosity = 0.6 for particle size of 50 and 100µm.

Since there exist a bend between zone 1 and zone 2, it was investigated whether the increase in deposition under increased velocities was due to the presence of either the porous media or the geometric bend itself. It can be argued that increase of velocity without the implementation of the porous media would contribute to an increase in particle deposition at the bend. However, an increase in inlet air velocity does not contribute to an increase in particle deposition at the bend as was observed by keeping the flow within laminar parameters. Though the geometrical factors of the vestibule catalyse to the deposition, the presence of porous regime, which acts as a momentum sink, increases the volumetric velocity, thereby causing recirculation that in turn contributes to the increase in deposition. The highest local deposition efficiency was found to be present at the porosity of 0.6 and was predicted to be around 20%. The highest total deposition of the entire domain was found to be 96% for the 0.6 porosity.

The most important observation for the deposition efficiency comes from the fact that the decrease in porosity favours a shift in deposition pattern towards the anterior region. This, however, is the effect of the difference of the inertial loss between the particles and the carrier gas. As the size of the particle increases, the deposition efficiency increases, however the increase in deposition efficiency is more pronounced only for the particle size of 10µm or more. In cases of particle size of less than 5µm, the deposition exhibits a similar trendline with little variation in the total deposition efficiency.

Simulations were also done for particles of 50 and 100µm, a sample of which is shown in Figure 4(b). The deposition of 50 microns and greater suggest that regardless of whether the medium is porous or non-porous the deposition was found to be prominent in the vestibule region of the nasal cavity. This occurrence was observed due to the fact that there was not enough acceleration of the particles and the gravitational force dominated over the inertial force. In any case this was found to be consistent with the experiments carried out by Cheng et al. (2001). The effect of secondary flow of the carrier gas on the particles could not be established, as all particles were deposited in zone 1 and 2 and no particles were found in zone 3 where recirculation occurs.

Though it was argued that the use of *k-ε* model for complex geometry such as the nasal cavity is not appropriate and generates serious errors, a realisable k-ε model was run with a flow rate of 30 l/min (for human running condition) to observe the characteristics of particle deposition. Figure 5 shows the local particle deposition for *k-ε* turbulence model. It can be observed that, as the porosity decreases, the deposition increases as was found with laminar flow, but with high deposition efficiency. Increased particle deposition towards the anterior region, as a result of porosity decrease, was also observed in turbulence model. These results are preliminary and therefore no conclusive argument was drawn to establish the validity of *k-ε* for the turbulence model.

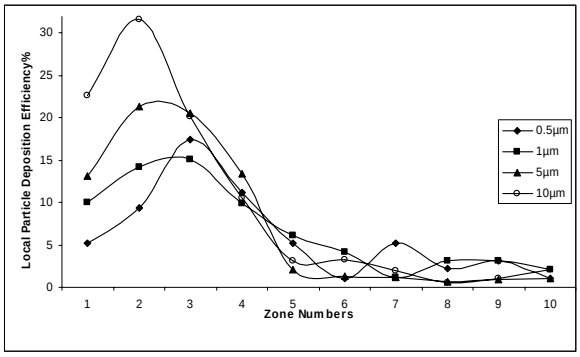

Figure 5. Local particle deposition efficiency for a turbulent flow at porosity = 0.6.

CONCLUSIONS

This CFD study examined the incorporation of a simple porous model to emulate the nasal hair growth by assuming virtual pore holes inside the vestibule region. Given the complexity of the geometry it was considered to include only laminar flow in the porous model. The results suggest that the inclusion of the porous model significantly increased both local and total deposition inside the nasal cavity and pharynx. For the non-porous model the velocity of the fluid and particles were found to decrease, but were found to increase in the porous model. Decrease in porosity contributes to an increase in deposition in the anterior region and also caused a forward shift in the pattern of the local deposition efficiency. The one-way coupling used in this model accounted for an inertial loss on the particle motion and that increased with an increase in particle size.

REFERENCES

Balashazy, I. and Hoffmann, W., (1993), Particle deposition in airway bifurcations-I. Inspiratory flow. *J. Aerosol Sci,* 24, 745-772.

Cheng, Y.S., Holmes, T.D., and Gao, J., (2001), Characterization of nasal spray pumps and deposition pattern in a replica of the human nasal airway. *J. Aerosol Med,* 14, 267-280.

Dukowicz, J.K., (1980), A particle-fluid numerical model for liquid sprays. *J. Comp Phy,* 35, 229-253.

Fluent Inc., (2003), Fluent User's Guide, release 6.1.22.

Frey, J.M., Schmitz, P., Dufreche, J., and Gohr Pinheriro, I., (1999), Particle deposition in porous media: analysis of hydrodynamic and weak inertial effects. *Transport in porous media,* 37, 25-54.

Gemci, T., Corcoran, T.E., and Chigier, N., (2000), Dispersion and deposition of inhalation therapy sprays in the larynx and trachea using experimental and numerical methods. *ICLASS-2000,* Pasadena, CA.

Gemci, T., Corcoran, T.E., and Chigier, N., (2002a), A numerical and experimental study of spray dynamics in a simple throat-model. *Aerosol Sci. Technol,* 36, 18–38.

Hahn, T., Scherer, P.W., and Mozell, M.M., (1993), Velocity profiles measured for air flow through a large-scale model of the human nasal cavity. *J. Appl. Physiol,* 75, 2273-2287.

Hofmann, W., Golser, R., and Balashazy, I., (2003), Inspiratory deposition efficiency of ultrafine particles in a human airway bifurcation model. *Aerosol Sci. Technol,* 37, 988-994.

Martonen, T.B., Zhang, Z., Yue, G., and Musante, C.J., (2002), 3-D particle transport within the human upper respiratory tract. *J. Aerosol Sci,* 33, 1095–1110.

Morsi, S.A., and Alexander, A.J., (1972), An investigation of particle trajectories in two-phase flow systems. *J. Fluid Mech.* 55, 193-208.

Mygind, N., and Dahl, R., (1998), Anatomy, physiology and function of the nasal cavities in health and disease. *Adv. Drug Delivery Rev,* 29, 3-12.

Naftali, S., Schroter, R.C., Shiner, R.J., and Elad, D., (1998), Transport phenomena in the human nasal cavity: A computational model. *Ann. Biomed. Eng,* 26, 831-839.

Schreck, S., Sullivan, K.J., Ho, C.M., and Chang, H.K., (1993), Correlations between flow resistance and geometry in a model of the human nose. *J. Appl. Physiol,* 75(4), 1767-1775.

Stapleton, K.W., Guentsch, E., Hoskinson, M.K., and Finlay, W.H. (2000), On the suitability of k–ε turbulence modeling for aerosol deposition in the mouth and throat. *J. Aerosol Sci,* 31(6), 739–749.

Tu, J.Y., (2000), Numerical investigation of particle flow behavior in particle-wall function. *Aerosol Sci. Technol*. 32, 509-526.

Zhang, Z., Kleinstreuer, C., and Kim, C.S., (2002), Micro-particle transport and deposition in a human oral airway model. *J. Aerosol Sci,* 33, 1635–1652.